Available online at www.sciencedirect.com
ScienceDirect
Journal of Solid State Chemistry 180 (2007) 1250–1258
JOURNAL OF SOLID STATE CHEMISTRY
www.elsevier.com/locate/jssc

Phase transition and mixed oxide-proton conductivity in germanium oxy-apatites

Laura León-Reina, José M. Porras-Vázquez, Enrique R. Losilla, Miguel A.G. Aranda*

Departamento de Química Inorgánica, Cristalografía y Mineralogía, Universidad de Málaga, 29071-Málaga, Spain

Received 1 December 2006; received in revised form 9 January 2007; accepted 12 January 2007
Available online 15 February 2007

Abstract

$La_{9.75}\square_{0.25}(Ge_6O_{24})O_{2.62}$ oxy-apatite shows a phase transition from triclinic to hexagonal symmetry at approximately 1020 K that has been characterised by high-temperature synchrotron X-ray and neutron powder diffraction, and ionic conductivity measurements. The crystal structure at 1073 K has been determined from joint Rietveld refinements of synchrotron X-ray and neutron powder diffraction data. The study shows that hexagonal-$La_{9.75}\square_{0.25}(Ge_6O_{24})O_{2.62}$ contains interstitial oxygen at the position previously reported for other oxy-germanates. Changes in the oxide conductivity associated with this structural transition are discussed. The thermal analyses showed a weight loss on heating close to 600 K very likely due to water release. The synchrotron thermodiffractometric study shows an anomaly in the cell parameters evolution at that temperature, which indicates that this residual water is located into the apatite channels. The electrical characterisation under different atmospheres (dry and wet synthetic air) indicates that there is a significant proton contribution to the overall conductivity below 600 K, mainly under wet atmosphere.
© 2007 Elsevier Inc. All rights reserved.

Keywords: Apatite; Synchrotron and neutron diffraction; Oxygen interstitial and proton conductivity

1. Introduction

Rare earth oxy-apatites are attracting considerable interest due to their high oxide ion conductivities and low activation energies [1,2], properties that are making these materials promising electrolytes for solid oxide fuel cells, SOFCs [3]. The initial works on rare earth apatite-type oxide ion conductors were focused on the Si system with two limiting stoichiometries: $Ln_{10}\square_0(SiO_4)_6O_3$ [4–6] and $Ln_{9.33}\square_{0.67}(SiO_4)_6O_2$ [7–12] (Ln = lanthanide); immediately after, related systems containing Ge at the tetrahedral site were published [13–17]. Then, different attempts to change/optimise the ionic conductivity of these materials were reported, including the replacement of La or Nd by Sr, Mg, Ca or Ba [18,19], the replacement of Si by Al, Ga, Zn or Fe [19–22], and the preparation of mixed Si–Ge derivatives [18,23,24].

The precise mechanistic features of oxygen ion transport in apatite-type materials were reported as theoretical predictions by Slater et al. [25,26] for $La_{9.33}\square_{0.67}(SiO_4)_6O_2$ and $La_8Sr_2(SiO_4)_6O_2$. The atomistic modelling proposed that the high ionic conductivity and low activation energy of $La_{9.33}\square_{0.67}(SiO_4)_6O_2$ was due to an interstitial-oxide mechanism with a sinusoidal-like pathway along the *c*-axis. Subsequently, some important contributions [7,22,27–31] to the knowledge of the relationship between structure and oxide conductivity have been published. The joint use of synchrotron or laboratory X-rays and neutron powder diffraction has allowed locating the interstitial oxide anions for hexagonal oxy-apatites in the position previously reported in the theoretical works [22,27–30]. Very recently, neutron powder diffraction studies for $La_{9.33}\square_{0.67}(Si_6O_{24})O_2$ [32] and Zn-doped derivative [22] firmly established the presence of interstitial-oxygen in oxygen-stoichiometric oxy-apatites with vacancies at the lanthanum sublattice.

There are several works showing that the conduction species are only oxide ions [17,28,33–35] because the ionic

*Corresponding author. Fax: +34 952 13 20 00.
E-mail address: g_aranda@uma.es (M.A.G. Aranda).

0022-4596/$ - see front matter © 2007 Elsevier Inc. All rights reserved.
doi:10.1016/j.jssc.2007.01.023

transference numbers obtained employing different techniques are very near to the unity (pure ionic conductor). However, the main drawback of apatites is the high temperature necessary to obtain dense pellets and the segregation of dielectric phases at the grain boundary. In order to decrease the sintering temperature some authors have doped the apatite structure with transition metal cations (Co, Fe, Mn, Ti) [20,21,36–38]. This procedure leads to compactions as high as 90%, although samples develop an n-type electronic contribution in reducing atmospheres. Besides the technological importance of apatites as oxide conductors, other investigations into the electrical properties for some apatites have been performed. For example, $Pb_6Ca_2A_2(PO_4)_6$ (A = Li, Na) [39] shows a remarkable cationic mobility. No evidences of mixed (anionic–cationic) conductivity have been reported so far.

The $La_{10-x}\square_x(GeO_4)_6O_{3-1.5x}$ apatite series were obtained as single phases in a narrow compositional range ($9.52 \leqslant 10-x \leqslant 9.75$). These apatites phases are hexagonal (space group, s.g., $P6_3/m$) for $9.52 \leqslant 10-x \leqslant 9.60$ and triclinic (s.g. P-1) for $9.66 \leqslant 10-x \leqslant 9.75$ at room temperature [17]. On heating, the triclinic cell transforms to a hexagonal cell over the 773–1123 K temperature range depending upon the apatite composition [40]. The aim of this work is to better characterise this high-temperature phase transition using high-resolution synchrotron powder diffraction. It is also intended to locate the interstitial oxygen in this oxygen excess compound, $La_{9.75}\square_{0.25}(Ge_6O_{24})O_{2.62}$, from neutron diffraction data. Furthermore, the electrochemical characterisation shows that both oxide and proton conductivities take place below 600 K.

2. Experimental

2.1. Synthesis

The synthesis of $La_{10-x}\square_x(GeO_4)_6O_{3-1.5x}$ ($10-x =$ 9.75, 9.66, 9.60 and 9.55) series was carried out by the solid state procedure previously reported [17]. These samples are highly crystalline single phases and, hereafter, labelled as La_{10-x}.

2.2. Powder diffraction

High-resolution synchrotron X-ray powder diffraction (SXRPD) patterns were collected on ID31 diffractometer (European Synchrotron Radiation Facility [ESRF], Grenoble, France) for $La_{9.75}$ sample. The measurements were done from room temperature to 1173 each 100 K. The sample was loaded in a borosilicate glass capillary (with a diameter of ~1 mm) and rotated during data collection. The measuring wavelength was $\lambda = 0.62075(1)$ Å (19.97 keV) selected with a double-crystal Si(1 1 1) monochromator and calibrated with Si standard from NIST ($a = 5.431195$ Å). The overall measuring time was ~40 min per pattern to have very good statistics over the angular range 2–30° (in 2θ) (11.5−0.77 Å). The data from the multi-analyser Si(1 1 1) stage were normalised and summed up to 0.003° step size with local software to produce the final raw data.

High-temperature neutron powder diffraction (HT-NPD) patterns were collected on HRPT diffractometer [41] (SINQ neutron source at Paul Scherrer Institut, Villigen, Switzerland) for $La_{9.75}$ sample. The measurement was done at 1073 K. The sample was loaded in a vanadium can and was connected to a vacuum pump. The wavelength, ~1.886 Å, was selected by the (5 1 1) reflection of the vertically focusing Ge monochromator. The overall measuring time was ≈6 h per scan to have good statistics over the 2θ angular range of 5–165° (21−0.95 Å) with 0.05° step size.

Full structural characterization at high temperature was carried out by a joint analysis of SXRPD and NPD data. All Rietveld analyses were done using the GSAS suite of programs [42].

2.3. Thermal analysis

Thermogravimetric analyses (TG) were performed on a Pyris–Diamond Perkin–Elmer apparatus. The temperature was varied from RT up to 1273 K at a heating/cooling rate of 10 K min^{-1} with a flux of atmospheric air of 80 cm^3 min^{-1} (provided by an air compressor), using a mass of ~70 mg. The TG instrument was calibrated using standard samples and the equipment baseline, measured with two empty crucibles, was subtracted. Two heating/cooling cycles were carried out to study the thermal reversibility and reproducibility of the measurements. Thermomechanical analysis (TMA) was carried out for $La_{9.75}$ on a NETZSCH Gerätebau 402 EP apparatus equipped with a silica support. The temperature was varied from RT up to 1273 K at a heating rate of 5 K min^{-1}. The measurements were done in a 5.8 mm long specimen with a residual porosity of 10%.

2.4. Electrical measurements

Electrical characterisation was carried out on cylindrical pellets (~5 mm of diameter and ~1 mm of thickness) obtained by pressing ~0.1 g of sample at 1000 MPa, for 5 min. The pellets were sintered at 1573 K for 6 h at a heating rate of 10 K min^{-1}. The pellets were not fully dense and the compactions ranged between 80% and 85% of the theoretical values (taking into account the pellets masses and volumes, and the crystallographic densities). Electrodes were made by coating opposite pellet faces with METALOR® 6082 platinum paste and gradually heating to 1073 K at a rate of 10 K min^{-1} in air to decompose the paste and harden the Pt residue. Successive treatments were made to achieve an electrical resistance of both pellets faces lower than 1 Ω.

Impedance spectroscopy data in two different flowing atmospheres (dry-air and wet-air) were collected using a

Hewlett-Packard 4284A impedance analyser over the frequency range 20 Hz–1 MHz from 533 to 1273 K for $La_{9.75}$ and at 570 K for $La_{9.55}$, $La_{9.60}$ and $La_{9.67}$ samples. Measurement processes were electronically controlled by the winDETA package of programs [43]. The pellets were mounted in a home made alumina conductivity jig, with four Pt wires shielded in two alumina tubes, which were placed in a tubular furnace. Electrical data were taken every 20 K. A delay time of 60 min at each temperature was selected to ensure thermal equilibrium. Temperatures were reproducible to ± 1 K.

3. Results and discussion

3.1. Structure evolution with temperature

The SXRPD patterns for $La_{9.75}$ do not change significantly up to 800 K but from 873 to 1073 K the degree of peak-splitting decreases and the intensity of the very sharp peaks notably increases. To illustrate that, Fig. 1 shows a selected region (18–19.6°/2θ) of the SXRPD patterns between 873 and 1173 K for $La_{9.75}$, where a phase transition is clearly visible between 973 and 1073 K. Below that transition, the SXRPD patterns were indexed on a triclinic cell, with cell parameters at 873 K: $a = 9.9764(2)$ Å, $b = 9.9696(1)$ Å, $c = 7.3313(1)$ Å, $\alpha = 90.511(1)°$, $\beta = 89.183(1)°$ and $\gamma = 120.271(1)°$. Above the transition, the SXRPD patterns were indexed on a hexagonal cell, with edges at 1073 K: $a = b = 9.9855(1)$ Å and $c = 7.3466(1)$ Å. However, the triclinic-to-hexagonal phase transition on heating at ~1020 K is not the only effect observed in the thermal evolution of the cell parameters of $La_{9.75}$, see Fig. 2. At temperatures close to 600 K, a clear anomaly is also observed in the unit cell parameters except the *c*-axis. This anomalous tiny change was not previously reported [40], which was likely due to the lack of resolution of the laboratory powder diffraction data.

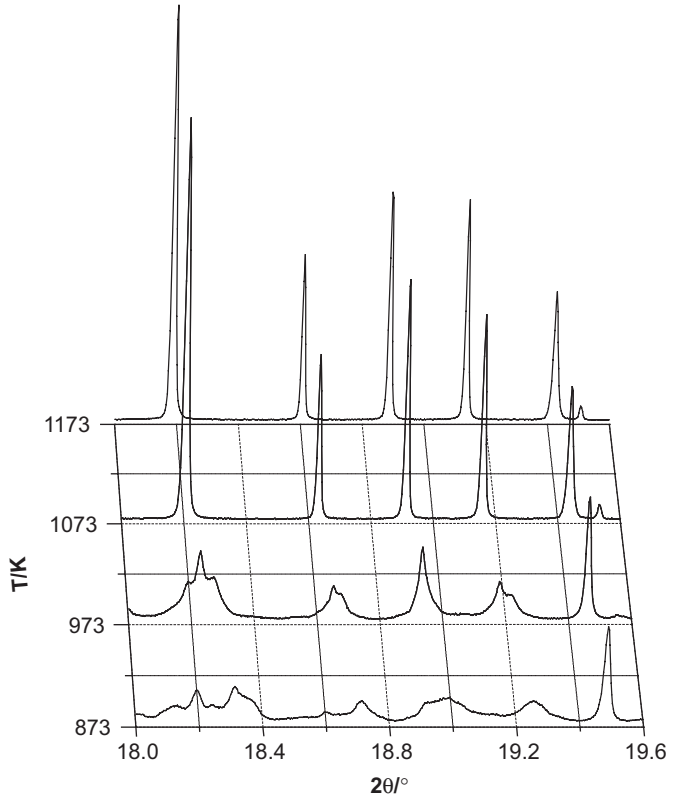

Fig. 1. Selected high-temperature synchrotron X-ray diffraction patterns for $La_{9.75}\square_{0.25}(Ge_6O_{24})O_{2.62}$.

To deeply investigate the effect at ~600 K, the sample was further studied by thermogravimetric analysis (TGA). Fig. 3 shows the TG curves (two consecutive cycles) taken under airflow for $La_{9.75}$. The first cycle shows a continuous weight loss up to 1300 K; however, the main effect is an abrupt weight loss close to 580 K. The mass loss associated to that step is 0.2% that can be due to water uptaken by the sample. Under this reasonable assumption, the water content of this sample must be close to 0.25 moles of H_2O per chemical formula, $La_{9.75}\square_{0.25}(Ge_6O_{24})O_{2.62}$. During the cooling process, the initial state is not fully recovered as the thermal analyses were carried out under atmospheric air flow at a rapid heating/cooling rate of 10 K min^{-1}, but a water uptake around 560 K is clearly observed. A second cycle for the TGA analysis was carried out to check the dynamic nature of the water uptake/release. Under these non-equilibrium conditions, the adsorbed/absorbed water is again released close to 580 K. These small, but abrupt, mass changes are not due to the equipment or to an improper correction of the baseline and they take place at the same temperature where the anomaly in the cell parameters evolution is detected. Taken together the SXRPD and TGA results, it can be said that germanium oxy-apatites reversibly absorb a small amount of water that it is released close to 600 K.

The volume thermal expansion coefficient for $La_{9.75}\square_{0.25}(Ge_6O_{24})O_{2.62}$ derived from HT-SXRPD patterns above 700 K, was $\alpha_v = 3.46(1) \times 10^{-5}$ K^{-1} (α_v is defined as m/n for the $V(T) = n + mT(K)$ fit). Under the isotropic thermal expansion approximation, the linear expansion coefficient, β_{calc}, can be derived as $\beta_{calc} = \alpha_v/3 = 11.5 \times 10^{-6}$ K^{-1}. The result of the TMA for the same material gave an average polycrystalline linear expansion coefficient value, $\beta_{meas} = 8.8 \times 10^{-6}$ K^{-1}. The difference between these two values is likely due to the residual porosity (12%) of the sintered bar used in the dilatometric study.

3.2. High-temperature crystal structure

The room-temperature triclinic structure of $La_{9.75}\square_{0.25}(Ge_6O_{24})O_{2.62}$ was already reported [17]. Here, only the structure at 1073 K is reported as the atomic parameters are obtained from a joint Rietveld [44] refinement of SXRPD and NPD data. The starting model was that earlier reported [27] for $La_{9.60}\square_{0.40}(Ge_6O_{24})O_{2.4}$ (at room temperature) in $P6_3/m$ space group. To describe the stoichiometry, the occupation factor for the lanthanum site was conveniently modified. We started the Rietveld

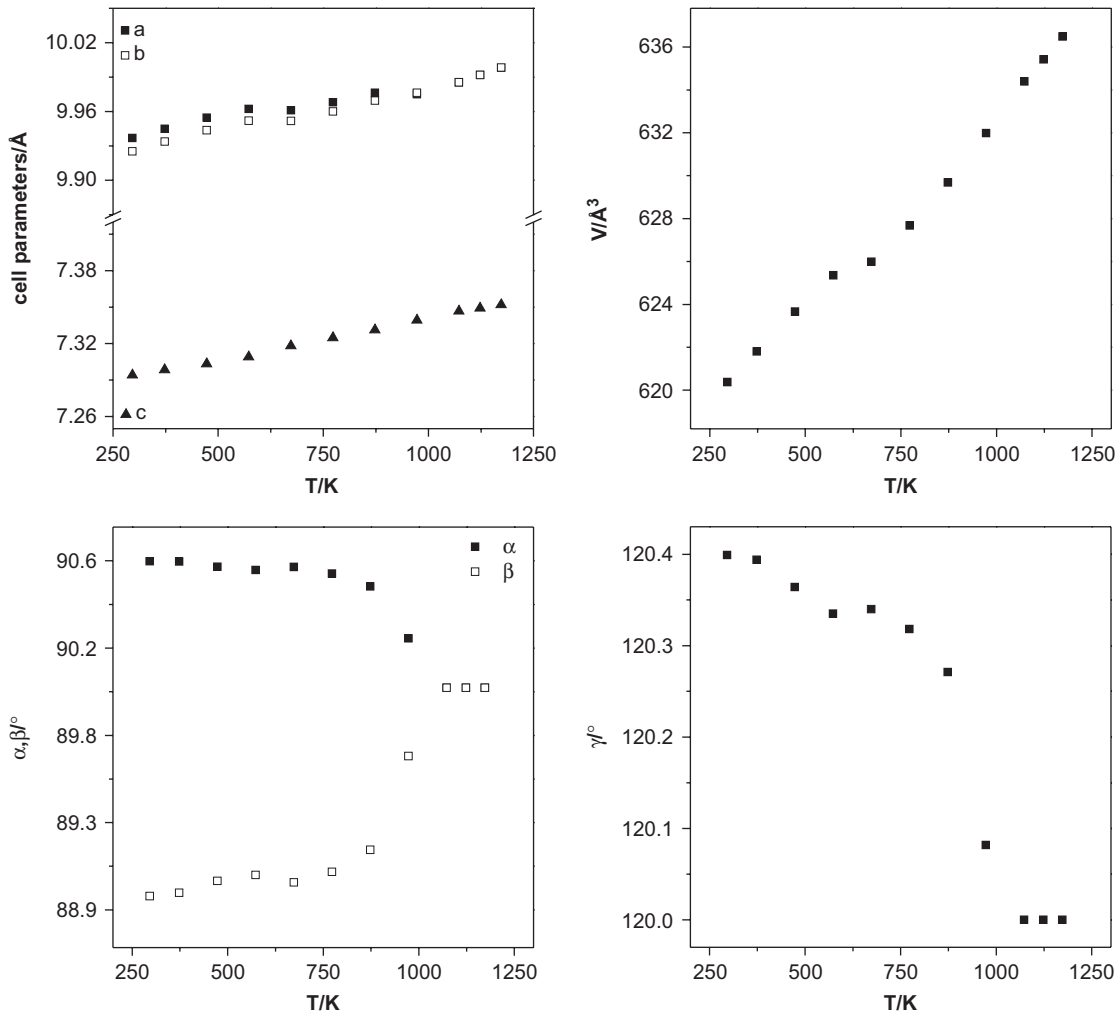

Fig. 2. Variation of the unit cell parameters with temperature for $La_{9.75}\square_{0.25}(Ge_6O_{24})O_{2.62}$ from high-resolution synchrotron X-ray powder diffraction data.

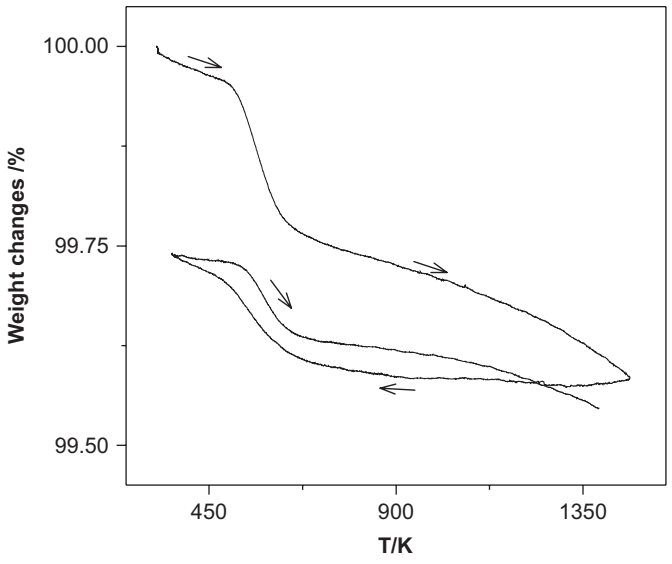

Fig. 3. Heating and cooling thermogravimetric curves (the processes are highlighted with arrows) for $La_{9.75}\square_{0.25}(Ge_6O_{24})O_{2.62}$. All measurements were carried out under atmospheric airflow.

refinement without the interstitial oxygen and hence, the initial stoichiometry was $La_{9.75}\square_{0.25}(Ge_6O_{24})O_2$, which is charge unbalanced. The usual parameters: histogram scale factors, background coefficient and peak shape coefficients were varied. The neutron wavelength was refined in the simultaneous analysis and converged to 1.8862(2) Å. The lanthanum vacancies have been located completely ordered at the nine-coordinated La(2) site, in full agreement with several previous NPD studies [see for instance Ref. 29].

At this stage, a difference Fourier-map was computed for the NPD histogram to locate the interstitial oxygen, O(5). The highest intense peak in the map was located at (0.01, 0.22, 0.63) with a height of 0.046 fm/Å^3, see Fig. 4. This peak coincides with the position previously reported for the interstitial-oxygen in several oxy-apatites from NPD [27–30,32] and predicted theoretically from atomistic simulations [25,26].

The sample is single phase, both by SXRPD and NPD, an so, we constrained the occupation factor of O(4), at the centre of the channels, with O(5), at the interstitial positions, to maintain the electroneutrality; yielding the

Fig. 4. Difference-Fourier map section at $z = 0.62$ for the computed stoichiometry, $La_{9.75}\square_{0.25}(Ge_6O_{24})O_{2.0}$, from neutron powder diffraction at 1073 K. The highlighted strongest peak is due to the excess-oxygen (interstitial site) in $La_{9.75}\square_{0.25}(Ge_6O_{24})O_{2.62}$.

refined occupation factors for O(5) given in Table 1. Atomic displacement parameters (ADPs) for all atoms except interstitial oxygens have been refined anisotropically. The thermal parameter for O(5) has been fixed to a reasonable value ($U_{iso} = 0.03\,Å^2$) because its very small occupation factor, see Table 1, does not allow to refine it. Final unit cell parameters, Rietveld disagreement factors, atomic positional parameters and occupation factors are given in Table 1 and the high-temperature anisotropic displacement factors are given in Table 2. The final SXRPD and NPD Rietveld plots are given in Fig. 5.

The reported anisotropic thermal parameters take into account the thermal vibration and the positional disorder due to the local lattice relaxation around the interstitial oxygens. It must be noted that the refined position of the interstitial oxygen, O(5), is very close to the average position of O(3) (~1.1 Å). However, atomistic calculations [25,26] have shown that the lattice can accommodate this interstitial oxygen through a local relaxation around these defects. The main parameter to detect this relaxation is U_{11} of O(3) which is as high as $11.0(1) \times 10^{-2}\,Å^2$ at 1073 K, see Table 2. This very large value reflects the local movement of some silicate groups (those very close to the few interstitial oxygens), as it has been previously pointed out for excess and stoichiometric-oxygen samples [30,32]. On

Table 1
Refined unit cell values, Rietveld disagreement factors, atomic positional parameters and occupation factors at 1073 K for $La_{9.75}\square_{0.25}(Ge_6O_{24})O_{2.62}$ in $P6_3/m$ space group

a/Å	9.9918(1)	R^X_{wp}/R^N_{wp}/%	5.94/3.60
c/Å	7.3493(1)	R^X_p/R^N_p/%	4.36/2.83
V/Å^3	635.42(1)	R^X_F/R^N_F/%	2.79/1.99

Atom	x	y	z	$U_{iso} \times 100$/Å^2	Occ. Fac.
La(1), 6*h*, (x y 1/4)	0.2283(1)	−0.0107(1)	1/4	2.24	1
La(2), 4*f*, (1/3 2/3 z)	1/3	2/3	0.0024(2)	2.95	0.9375
Ge, 6*h*, (x y 1/4)	0.4020(1)	0.3741(1)	1/4	1.74	1
O(1), 6*h*, (x y 1/4)	0.3166(2)	0.4905(2)	1/4	4.94	1
O(2), 6*h*, (x y 1/4)	0.6016(2)	0.4724(2)	1/4	4.21	1
O(3), 12*i*, (x y z)	0.3433(2)	0.2517(1)	0.0622(1)	6.70	1
O(4), 2*a*, (0 0 1/4)	0	0	1/4	5.75	0.913(5)
O(5), 12*i*, (x y z)	0.015(2)	0.229(2)	0.618(2)	3[a]	0.067(1)

[a]Fixed.

Table 2
Refined anisotropic thermal parameters at 1073 K for $La_{9.75}\square_{0.25}(Ge_6O_{24})O_{2.62}$ in $P6_3/m$ space group

Atoms	$U_{11} \times 100$	$U_{22} \times 100$	$U_{33} \times 100$	$U_{12} \times 100$	$U_{13} \times 100$	$U_{23} \times 100$
La(1), 6*h*, (x y 1/4)	2.5(1)	1.6(1)	2.6(1)	0.8(1)	0	0
La(2), 4*f*, (1/3 2/3 z)	3.6(1)	3.6(1)	1.6(1)	1.8(1)	0	0
Ge, 6*h*, (x y 1/4)	1.5(1)	1.5(1)	2.2(1)	0.7(1)	0	0
O(1), 6*h*, (x y 1/4)	6.5(1)	4.8(1)	3.5(1)	5.0(1)	0	0
O(2), 6*h*, (x y 1/4)	2.0(1)	3.5(1)	7.0(1)	1.7(1)	0	0
O(3), 12*i*, (x y z)	11.0(1)	5.0(1)	4.1(1)	5.4(1)	−3.9(1)	−2.3(1)
O(4), 2*a*, (0 0 1/4)	0.7(1)	0.7(1)	15.9(4)	0.3(1)	0	0

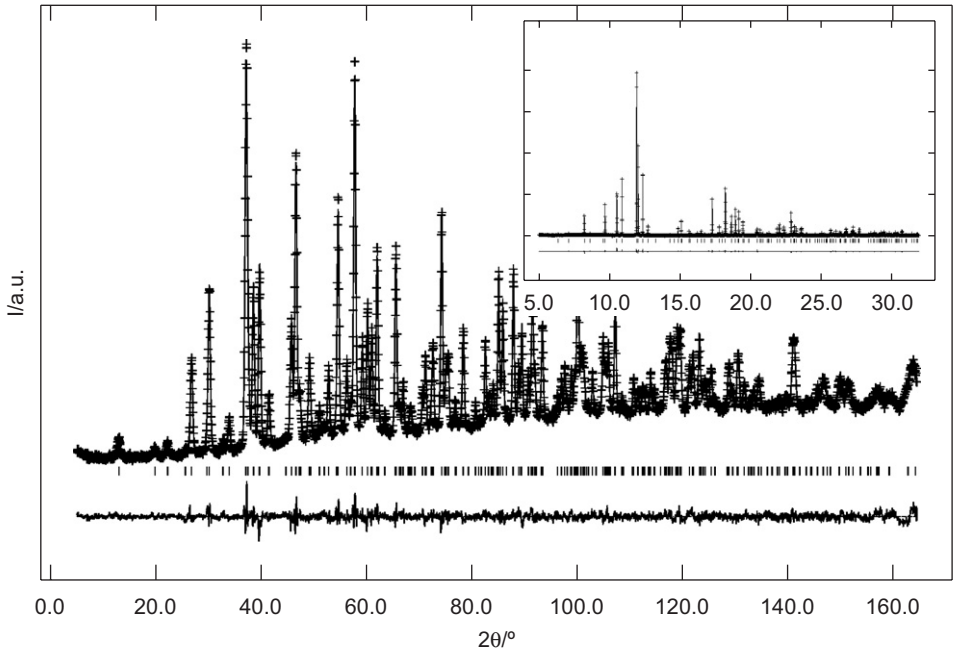

Fig. 5. Observed (crosses), calculated (full line) and difference (bottom) NPD for $La_{9.75}\square_{0.25}(Ge_6O_{24})O_{2.62}$ at 1073 K. The inset shows a selected SXRPD region for the same sample at the same temperature.

the other hand, the thermal parameter of O(4) along the *c*-direction (U_{33}), see Table 2, is huge which strongly suggests oxygen mobility along the channel.

3.3. Electrical characterization

3.3.1. High temperature conductivity behaviour

Fig. 6 shows the Arrhenius plot ($\ln(\sigma T)$ vs. $1000/T$) for $La_{9.55}\square_{0.45}(Ge_6O_{24})O_{2.32}$ and $La_{9.75}\square_{0.25}(Ge_6O_{24})O_{2.62}$, where the data have been normalised to the values at 582 K. For $La_{9.55}\square_{0.45}(Ge_6O_{24})O_{2.32}$, a soft curvature at high temperature towards smaller activation energies is observed in the Arrhenius plot on heating. This behaviour is commonly observed for compounds with high ionic conductivities. This curvature is usually explained by the presence of a critical temperature T_c [45], below which the oxygen vacancies are progressively trapped out into the clusters with decreasing temperature. Above T_c, the vacancies are dissolved into the matrix of oxygen sites. This explanation was initially envisaged [45] for oxide-conductors with oxygen-vacancies as main conduction mechanism. However, it can be extended to an interstitial-oxygen mechanism by assuming that below T_c, the interstitial oxygens are progressively trapped out into clusters. Above T_c, the interstitial oxygens are progressively dissolved into the matrix of oxygen sites. The plot shown in Fig. 6 indicates that T_c is 970 K for $La_{9.55}\square_{0.45}(Ge_6O_{24})O_{2.32}$. It must be noticed that all measured values are arranged into two straight lines intersecting at T_c, as expected [45].

The Arrhenius plot for $La_{9.75}\square_{0.25}(Ge_6O_{24})O_{2.62}$, see also Fig. 6, shows a related but not identical behaviour.

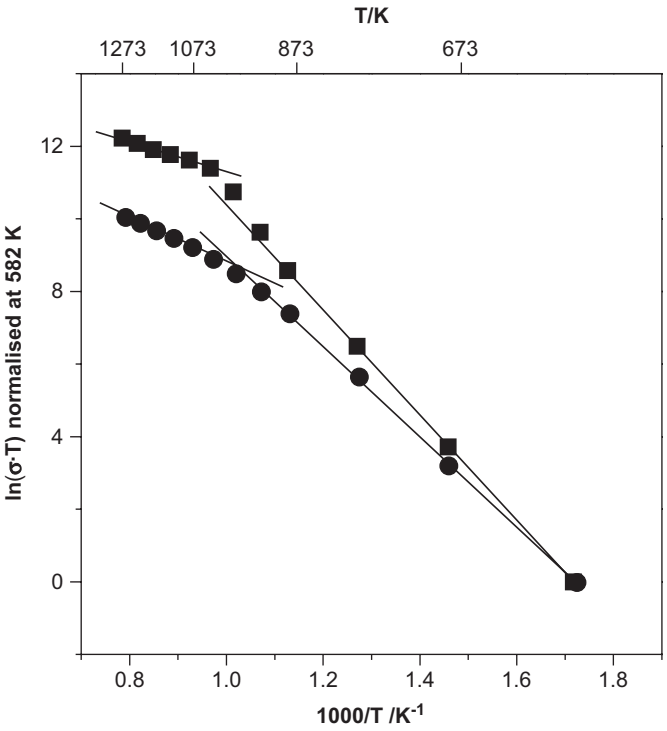

Fig. 6. Arrhenius plots ($\ln(\sigma T)$ vs. $1/T$) for $La_{9.55}\square_{0.45}(Ge_6O_{24})O_{2.32}$ (solid circles) and $La_{9.75}\square_{0.25}(Ge_6O_{24})O_{2.62}$ (solid squares). The plots have been normalised to the values of σT at 582 K to help the visualisation of the different behaviour of the two samples.

Two regimes with very different activation energies are also observed. However, it must be noticed that the Arrhenius plot does not give two straight lines intersecting at T_c.

Conversely, the low-temperature straight line lies well below that corresponding to the high-temperature 'unclustered' regime. This behaviour is a clear signature of the triclinic-to-hexagonal phase transition that takes place close to 1020 K. The critical temperature, T_c, for $La_{9.55}\square_{0.45}(Ge_6O_{24})O_{2.32}$, ~970 K, is intimately related with the transition temperature for the triclinic–hexagonal transformation for $La_{9.75}\square_{0.25}(Ge_6O_{24})O_{2.62}$, ~1020 K. The main difference is that the interstitial oxygen trapping at low temperatures for $La_{9.75}$, below 1020 K, provokes a long-range distortion, which decreases the lattice symmetry from hexagonal to triclinic, on cooling.

3.3.2. Intermediate temperature conductivity behaviour

The water uptake in $La_{9.75}\square_{0.25}(Ge_6O_{24})O_{2.62}$ detected by TGA points toward the possibility of a proton contribution to the total conductivity below 600 K. To investigate this possibility, a study by impedance spectroscopy under dry and wet atmospheres was carried out. Proton conductivity has been repeatedly reported in oxide materials. For example, complex oxides with perovskite structure such as $BaCeO_3$-based compounds [46], $SrZrO_3$ [47], $Ba_2In_2O_5$-based materials [48] and $La_4(Ga_{2-x}Ti_xO_{7+x/2}\square_{1-x/2})O_2$ cuspidines [49] present variable proton conductivity in humidified atmospheres.

Fig. 7a shows the impedance spectra at 570 K for $La_{9.75}$ under a constant flow of dry and wet synthetic air (pellet compaction 85%). It is obvious from that figure that the total resistivity under wet air was lower than that under dry atmosphere. The reduction of the resistivity by increasing water partial pressure confirmed the appearance of proton conductivity in this system. The conductivity in wet air is almost half an order of magnitude larger than that in dry air below 600 K.

The Arrhenius plots of the total conductivities for $La_{9.75}$ are shown in Fig. 7b under both dry and wet atmospheres. The conductivity results are in very good agreement with the TG study, since above ~650 K, the proton conductivity is negligible. At temperatures lower than 600 K, the proton contribution to the overall conductivity is significant. The activation energy above 650 K is 1.06(1) eV, which is typical of oxide conductors. Below 600 K under wet atmosphere, the activation energy is 0.68(2) eV, which is typical of mixed proton–oxide conductors. Therefore, the curvature in the Arrhenius plot under wet atmosphere is explained as a consequence of the change in the conduction mechanism from mixed ionic (proton and oxide) below ~600 K to a predominantly oxide conductor above that temperature.

Impedance data were isothermally collected, at 570 K, in dry and wet air for the $La_{10-x}\square_x(GeO_4)_6O_{3-1.5x}$ ($9.55 \leqslant 10-x \leqslant 9.75$) series, see Fig. 8. The total conductivity values under wet air are invariably larger than those obtained under dry air. The conductivity evolution along

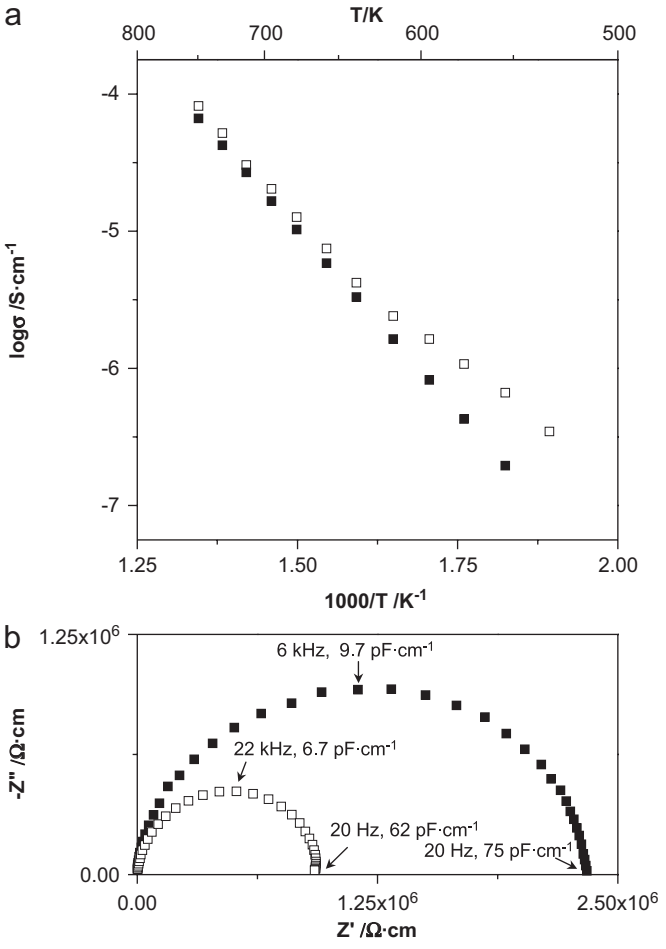

Fig. 7. (a) Complex impedance plane plots for $La_{9.75}\square_{0.25}(Ge_6O_{24})O_{2.62}$ at 570 K under two atmospheres, dry (solid squares) and wet (open squares) synthetic air. (b) Arrhenius plots ($\log\sigma$ vs. $1/T$) for the same sample and measuring conditions.

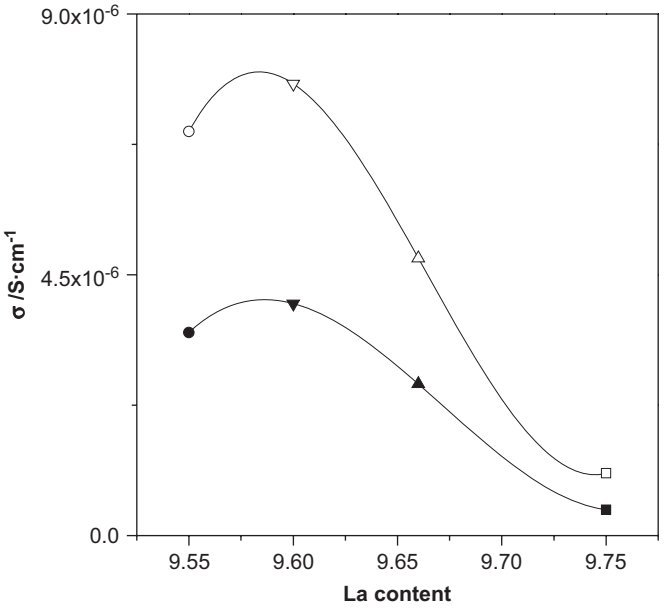

Fig. 8. Total conductivities at 570 K under dry (full symbols) and wet (open symbols) air for all compositions of $La_{10-x}\square_x(GeO_4)_6O_{3-1.5x}$ ($9.55 \leqslant 10-x \leqslant 9.75$) series. The lines are guide to the eyes.

the series is similar for both atmospheres. However, the proton contribution to the overall conductivity is larger for $La_{9.55}$ and $La_{9.60}$ likely due to a higher amount of lanthanum vacancies, which may helps the water uptake.

4. Conclusions

HT-SXRPD data for $La_{9.75}\square_{0.25}(Ge_6O_{24})O_{2.62}$ reveals a triclinic to hexagonal phase transition on heating close to 1020 K. The joint refinement of SXRPD and NPD data collected at 1073 K gave an accurate description of the hexagonal structure including the interstitial oxides at the same position previously reported for other oxy-apatites. The temperature-variable SXRPD study also shows an anomalous lattice behaviour at 600 K, which is due to water release out of the apatite structure. The impedance study under dry and wet atmospheres indicates that $La_{10-x}\square_x(GeO_4)_6O_{3-1.5x}$ compounds display appreciable proton conductivities below 600 K, mainly under wet atmospheres. Above 600 K, $La_{10-x}\square_x(GeO_4)_6O_{3-1.5x}$ materials are pure oxide conductors.

5. Supplementary material

Further details of the crystal structure investigation can be obtained from the Fachinformationszentrum Karlsruhe, 76344 Eggenstein-Leopoldshafen, Germany, (fax: (49) 7247-808-666; e-mail: crysdata@fiz.karlsruhe.de) on quoting the depository number CSD-417387.

Acknowledgments

The work in Málaga has been supported by the MAT2003-07483-C2-1 research grant. LLR and JMPV thank Junta de Andalucía and MEC, respectively, for two studentships. ESRF is thanked for the provision of X-ray synchrotron facilities at ID31. This work was partially performed at the spallation neutron source SINQ, Paul Scherrer Institut, Villigen, Switzerland.

References

[1] V.V. Kharton, F.M.B. Marques, A. Atkinson, Solid State Ionics 174 (2004) 135–149.
[2] F.M.B. Marques, V.V. Kharton, Ionics 11 (2005) 321–326.
[3] T. Ishihara, N.M. Sammes, O. Yamamoto, in: S.C. Singhal, K. Kendall (Eds.), High Temperature Solid Oxide Fuel Cells: Fundamentals, Design and Applications, Elsevier Ltd., Kidlington-Oxford, 2003 pp. 83–117.
[4] S. Nakayama, T. Kageyama, H. Aono, Y. Sadaoka, J. Mater. Chem. 5 (1995) 1801–1805.
[5] S. Nakayama, M. Sakamoto, J. Eur. Ceram. Soc. 18 (1998) 1413–1418.
[6] S. Tao, J.T.S. Irvine, Mater. Res. Bull. 36 (2001) 1245–1258.
[7] J.E.H. Sansom, D. Richings, P.R. Slater, Solid State Ionics 139 (2001) 205–210.
[8] M. Higuchi, H. Katase, K. Kodaira, S. Nakayama, J. Crystal Growth 218 (2000) 282–286.
[9] S. Nakayama, M. Sakamoto, M. Higuchi, K. Kodaira, M. Sato, S. Kakita, T. Suzuki, K. Itoh, J. Eur. Ceram. Soc. 19 (1999) 507–510.
[10] M. Higuchi, K. Kodaira, S. Nakayama, J. Crystal Growth 216 (2000) 317–321.
[11] M. Higuchi, K. Kodaira, S. Nakayama, J. Crystal Growth 207 (1999) 298–302.
[12] U. Kolitsch, H.J. Seifert, F. Aldinger, J. Solid State Chem. 120 (1995) 38–42.
[13] H. Arikawa, H. Nishiguchi, T. Ishirara, Y. Takita, Solid State Ionics 136 (2000) 31–38.
[14] J.E.H. Sansom, L. Hildebrandt, P.R. Slater, Ionics 8 (2002) 155–209.
[15] P. Berastegui, S. Hull, F.J. García, J. Grins, J. Solid State Chem. 168 (2002) 294–305.
[16] S. Nakayama, M. Sakamoto, J. Mater. Sci. Lett. 20 (2001) 1627–1629.
[17] L. León-Reina, M.C. Martín-Sedeño, E.R. Losilla, A. Cabeza, M. Martínez-Lara, S. Bruque, F.M.B. Marques, D.V. Sheptyakov, M.A.G. Aranda, Chem. Mater. 15 (2003) 2099–2108.
[18] P.R. Slater, J.E.H. Sansom, Solid State Phen. 90–91 (2003) 195–200; E. Kendrick, J.E.H. Sansom, J.R. Tolchard, M.S. Islam, P.R. Slater, Faraday Discuss. (2007) available on-line.
[19] A. Najib, J.E.H. Sansom, J.R. Tolchard, M.S. Islam, P.R. Slater, Dalton Trans. 19 (2004) 3106–3109.
[20] A.A. Yaremchenko, A.L. Shaula, V.V. Kharton, J.C. Waerenborgh, D.P. Rojas, M.V. Patrakeev, F.M.B. Marques, Solid State Ionics 171 (2004) 51–59.
[21] V.V. Kharton, A.L. Shaula, M.V. Patrakeev, J.C. Waerenborgh, D.P. Rojas, N.P. Vyshartko, E.V. Tsipis, A.A. Yaremchenko, F.M.B. Marques, J. Electrochem. Soc. 151 (2004) a1236–a1246.
[22] E. Kendrick, M.S. Islam, P.R. Slater, Solid State Ionics 177 (2006) 3411–3416.
[23] J.E.H. Sansom, P.R. Slater, Solid State Ionics 167 (2004) 23–27.
[24] J.E.H. Sansom, A. Najib, P.R. Slater, Solid State Ionics 175 (2004) 353–355.
[25] M.S. Islam, J.R. Tolchard, P.R. Slater, Chem. Commun. (2003) 1486–1487.
[26] J.R. Tolchard, M.S. Islam, P.R. Slater, J. Mater. Chem. 13 (2003) 1956–1961.
[27] L. León-Reina, E.R. Losilla, M. Martínez-Lara, S. Bruque, M.A.G. Aranda, J. Mater. Chem. 14 (2004) 1142–1149.
[28] L. León-Reina, E.R. Losilla, M. Martínez-Lara, M.C. Martín-Sedeño, S. Bruque, P. Núñez, D.V. Sheptyakov, M.A.G. Aranda, Chem. Mater. 17 (2005) 596–600.
[29] L. León-Reina, E.R. Losilla, M. Martínez-Lara, S. Bruque, A. Llobet, D.V. Sheptyakov, M.A.G. Aranda, J. Mater. Chem. 15 (2005) 2489–2498.
[30] L. León-Reina, J.M. Porras-Vázquez, E.R. Losilla, M.A.G. Aranda, Solid State Ionics 177 (2006) 1307–1315.
[31] H. Okudera, A. Yoshiasa, Y. Masubuchi, M. Higuchi, S. Kikkawa, J. Solid State Chem. 177 (2004) 4451–4458.
[32] L. León-Reina, J.M. Porras-Vázquez, E.R. Losilla, D.V. Sheptyakov, A. Llobet, M.A.G. Aranda, Dalton Trans. (2007) submitted for publication.
[33] A.L. Shaula, V.V. Kharton, F.M.B. Marques, J. Solid State Chem. 178 (2005) 2050–2061.
[34] A.L. Shaula, V.V. Kharton, F.M.B. Marques, Solid State Ionics 177 (2006) 1725–1728.
[35] N. Takeda, Y. Itagaki, H. Aono, Y. Sadaoka, Sensors Actuators B 115 (2005) 455–459.
[36] J. Mcfarlane, S. Barth, M. Swaffer, J.E.H. Sansom, P.R. Slater, Ionics 8 (2002) 149–154.
[37] A.L. Shaula, V.V. Kharton, J.C. Waerenborgh, D.P. Rojas, E.V. Tsipis, N.P. Vyshartko, M. Patrakeev, F.M.B. Marques, Mater. Res. Bull. 39 (2004) 763–773.
[38] A.L. Shaula, V.V. Kharton, J.C. Waerenborgh, D.P. Rojas, F.M.B. Marques, J. Eur. Ceram. Soc. 25 (2005) 2583–2586.
[39] (a) T. Naddari, H. El feki, J.M. Savariault, P. Salles, A.B. Salah, Solid State Ionics 158 (2003) 157–166;
(b) T. Naddari, J.M. Savariault, H. El feki, P. Salles, A.B. Salah, J. Solid State Chem. 166 (2002) 237–244.

[40] E.J. Abram, C.A. Kirk, D.C. Sinclair, A.R. West, Solid State Ionics 176 (2005) 1941–1947.
[41] P. Fischer, G. Frey, M. Koch, M. Konnecke, V. Pomjakushin, J. Schefer, R. Thut, N. Schlumpf, R. Burge, U. Greuter, S. Bondt, E. Berruyer, Physica B 146 (2000) 276–278.
[42] A.C. Larson, R.B. Von Dreele, GSAS program, Los Alamos National Lab. Rep. No. LA-UR-86748, 1994.
[43] Windeta, Novocontrol gmbh, Hundsangen, Germany, 1995.
[44] H.M. Rietveld, J. Appl. Crystallogr. 2 (1969) 65–71.
[45] K. Huang, R.S. Tichy, J.B. Goodenough, J. Am. Ceram. Soc. 81 (1998) 2565–2575.
[46] H. Iwahara, H. Uchida, K. Ono, J. Ogaki, Electrochem. Soc. 135 (1988) 529–532.
[47] T. Yajima, H. Susuki, T. Yogo, H. Iwahara, Solid State Ionics 51 (1992) 101–107.
[48] G.B. Zhang, D.M. Smyth, Solid State Ionics 82 (1995) 153–160.
[49] M.C. Martín-Sedeño, D. Marrero-López, E.R. Losilla, L. León-Reina, S. Bruque, P. Núñez, M.A.G. Aranda, Chem. Matter. 17 (2005) 5989–5998.